The Power of Single and Multibeam Two-Photon Microscopy for High-Resolution and High-Speed Deep Tissue and Intravital Imaging

Raluca Niesner,*† Volker Andresen,‡ Jens Neumann,§ Heinrich Spiecker,‡ and Matthias Gunzer*
*Helmholtz Centre for Infection Research, Junior Research Group Immunodynamics, D-38124 Braunschweig, Germany; †Institute of Physical and Theoretical Chemistry, Technical University of Braunschweig, D-38106 Braunschweig, Germany; ‡LaVision Biotec GmbH, 33607 Bielefeld, Germany; and §Institute for Applied Neuroscience, 39120 Magdeburg, Germany

ABSTRACT Two-photon microscopy is indispensable for deep tissue and intravital imaging. However, current technology based on single-beam point scanning has reached sensitivity and speed limits because higher performance requires higher laser power leading to sample degradation. We utilize a multifocal scanhead splitting a laser beam into a line of 64 foci, allowing sample illumination in real time at full laser power. This technology requires charge-coupled device field detection in contrast to conventional detection by photomultipliers. A comparison of the optical performance of both setups shows functional equivalence in every measurable parameter down to penetration depths of 200 μm, where most actual experiments are executed. The advantage of photomultiplier detection materializes at imaging depths $>$300 μm because of their better signal/noise ratio, whereas only charge-coupled devices allow real-time detection of rapid processes (here blood flow). We also find that the point-spread function of both devices strongly depends on tissue constitution and penetration depth. However, employment of a depth-corrected point-spread function allows three-dimensional deconvolution of deep-tissue data up to an image quality resembling surface detection.

INTRODUCTION

Fluorescence microscopy is an important tool in biomedical research for the study of tissues, cells, and even subcellular structures with high spatial and temporal resolution (1). As a result, the dynamics of live cells form the focus of many approaches. To avoid alterations induced by isolation from their natural environment, observing cellular behavior in living animals has become the preferred method for these analyses (2). The possibility of investigating cells in their natural environment is considered to be crucial for understanding their functions and behavior (2–4). Conventional wide-field or confocal intravital fluorescence microscopy can be applied to investigate blood flow in superficial vessels (3) or the migration of cells in subcapsular zones of peripheral lymph nodes (5). Often, however, the biologically most interesting phenomena such as T-cell activation happen 100–400 μm below the surface of relevant tissues in mice. The excitation wavelengths typically used in confocal microscopy hardly allow the examination of cells this deep in living tissue or whole animals. As a result of significant scattering and absorption occurring in optically dense samples, only a few times 10 μm can be investigated at the microscopic level. Therefore, cutting the object into slices is often the only method to obtain information about cell dynamics inside (6,7).

The invention of multiphoton microscopy (MPM) (8) represents a breakthrough in tissue and intravital studies. It substantially enlarges the penetration depth to a couple of hundred micrometers, thus enabling noninvasive imaging with subcellular resolution in intact animals (9). In addition to its larger penetration depth, MPM provides inherent optical sectioning, reduced photobleaching and photodamage outside the focal plane, and convenient excitation of UV-absorption bands of intrinsic fluorophors (7). Despite its subcellular resolution, MPM is also able to record simultaneous activity of multiple neurons in vivo by means of field detection of calcium currents (10). Although it has been widely used in neurology since its introduction more than 15 years ago (8), only in the last 5 years have immunologists also ''discovered'' MPM for their questions. Since then a huge number of publications (recently reviewed (4,9,11,12)) found multiple novel insights into the biophysics of cell migration and cell-cell communication under different conditions. Thus, given the obvious success of the technology, it can be expected that many more groups will start to set up MPM capabilities. To this end, a very informative review has summarized the advances and problems of MPM in the immunology field so far (11).

The most important drawback of MPM is probably that the two-photon-excitation efficiency of most fluorophors is very low compared to single-photon excitation, resulting in a small

Submitted December 5, 2006, and accepted for publication May 29, 2007.

R.N. and V.N. contributed equally to this work. R.N., V.A., and M.G. performed experiments, conceived the work, and wrote the paper. J.N. provided vital material. R.N., V.A., H.S., and M.G. analyzed and interpreted the data. M.G. supervised the work.

Address reprint requests to Matthias Gunzer, PhD, Helmholtz Centre for Infection Research, Junior Research Group Immunodynamics, Inhoffenstrasse 7, D-38124 Braunschweig Germany. Tel.: 49-531-6181-3130; Fax: 49-531-6181-3199; E-mail: mgunzer@helmholtz-hzi.de; or to Raluca Niesner, PhD, Technical University of Braunschweig, Institute of Physical and Theoretical Chemistry, Hans-Sommer Strasse 10, D-38106 Braunschweig, Germany. Tel.: 49-531-391-5346; Fax: 49-531-391-5396; E-mail: raluca.niesner@tu-bs.de.

Editor: Petra Schwille.

0006-3495/07/10/2519/11 $2.00

doi: 10.1529/biophysj.106.102459

number of emitted photons (13). This in turn leads to long image acquisition times that are often on the order of seconds, restricting observation of living samples and dynamic processes within them with a high temporal resolution. A common approach to overcome this problem is to increase the excitation laser power to generate more fluorescence and use faster scanning methods such as acousto-optical deflectors (9,11). But because the nonlinear photo damage rises faster than the number of excited molecules with increasing laser power (7), crossing a critical power level does not make sense. Thus, the only method to increase the number of fluorescence photons per time without raising photodamage is to parallelize the excitation process. Simultaneous excitation with N foci results in N times more excited molecules, which in turn enables N times quicker acquisition or much gentler imaging.

We employ here a multiphoton scanhead that makes use of reflecting mirrors to split an incoming infrared laser beam into a line of up to 64 beamlets (14). This scanhead makes it possible to generate up to 64 times more fluorescence light out of a sample compared to single-beam scanning systems without the danger of photo- or thermotoxicity. Consequently, scanning can be made up to 64 times faster, allowing real-time observation of image planes deep inside the sample with low power in each single focus. Because this setup is dependent on charge-coupled device (CCD)-camera field detection, it is necessary to evaluate its optical performance. The reference detection device here is a point detector (photomultiplier tube, PMT), which is used by switching the beam path inside the same scanhead to generate only a single excitation beam. Both methods are directly compared in terms of resolution, maximum penetration depth, and signal/noise ratio (SNR).

Another serious problem of tissue two-photon microscopy is the significant decrease of the optical resolution with increasing penetration depth. Novel approaches apply point-spread function (PSF) engineering by means of deformable mirrors, which, however, is technically challenging (15). Our experiments show that this is based on degradation of the excitation PSF caused by the transit through optically dense samples that feature a strongly varying refraction index. This prevents the resolution of small details deeper inside the sample. We demonstrate that the level of degradation of the PSF is strongly dependent on the type of tissue imaged and that application of a depth-dependent PSF for three-dimensional deconvolution completely restores maximum image quality.

METHODS

Multifocal two-photon microscope

All experiments were carried out using a specialized two-photon microscope that is based on a commercial scan head (TriMScope, LaVision BioTec, Bielefeld, Germany, Supplementary Fig. 1). We used either CCD cameras or photomultipliers for detection (14).

Agarose films

A 4% (wt %) aqueous suspension of agarose (Merck, Darmstadt, Germany) was boiled and then mixed with a 0.002% suspension of fluorescent polystyrene beads (emission maximum 440 nm and 515 nm, Invitrogen, Karlsruhe, Germany). The volume ratio of the suspensions was 7:3. The still-fluid mixture was quickly pipetted onto a glass slide and cooled down to room temperature to solidify.

Preparation of lymph nodes

A total of 25 μl of a 2% suspension of green fluorescent polystyrene beads was injected into the footpad of 8-week-old BALB/c mice (Harlan, Germany). Overnight, the beads moved into the popliteal lymph nodes. Mice were sacrificed, and the lymph nodes were isolated and used for experiments concerned with the analysis of spatial resolution.

Preparation of brain slices

Organotypic hippocampal brain slices (OHBS) were prepared as described (30) from 10-day-old transgenic B6.Cg-TgN (Thy1-YFP)16Jrs mice (Jackson, distributed by Charles River, Wilmington, MA), which express EYFP at high levels in subsets of neurons, including the pyramidal cells of the hippocampus (31). Hippocampi were dissected and transversely sliced into a 500-μm or a 700-μm thickness on a McIlwain tissue chopper (The Mickle Laboratory Engineering, Surrey, UK). OHBS were immediately fixed with 4% PFA for 40 min at room temperature and were maintained in 30% sucrose. OHBS were then cryosectioned to suitable thickness as described (30). Before usage, OHBS were rinsed in phosphate-buffered saline (PBS) for 3×10 min.

To determine the ePSF in OHBS, we kept 100 μl of a suspension of fluorescent beads (as used above within agarose) on each side of OHBS for 3–4 h at 37°C. This 100 μl of suspension was obtained by diluting a 2 wt % stock suspension of beads 1:1000 with water and adding 15 vol % DMSO. Under these conditions we could not observe any damage to the morphology of the samples. After the incubation with bead suspension, the OHBS were washed so that no bead clusters remained on the sample surface.

Intravital microscopy

Mice were prepared for intravital microscopy using Isofluran-based intubation narcosis and gentle exposure of the inguinal lymph node as described (5). Blood-flow measurements were performed on blood vessels above the inguinal lymph node. For blood staining, anesthetized mice were injected i.v. with 100 μl Rhodamine-6G (1.25 mM in 0.9% NaCl). Subsequently, spleen cells stained with CFSE (5 μM) or CTO (5 μM) were also injected i.v. Imaging was performed until 1h after injection, when the Rhodamine signal was beginning to decay.

The animal experiments were approved by the Gewerbeaufsichtsamt Braunschweig under file number 509.42502/07-04.04 and were performed in accordance with current guidelines and regulations.

RESULTS

For single-beam imaging, PMTs were used to detect the fluorescence, whereas in multibeam mode CCD cameras were employed. Consequently, the comparison between these two different methods is also a comparison of the optical performance between a pixel-by-pixel and a field-detection device.

Calibration and benchmarking of the measurement system

The optical performance of an imaging system for biological tissues is defined by its maximum spatial (lateral and axial) resolution, the maximum penetration depth, and the depth-dependent signal/noise ratio (ddSNR). Thus, we first investigated these parameters using an agarose gel as a model for a homogeneous sample.

The spatial resolution of a laser-scanning microscope is determined by the dimensions of the effective (detected) point-spread function (ePSF) of a punctiform object with dimensions below the resolution limit. The rigorous mathematical description of the PSF is complicated (16–19). A commonly accepted procedure is to approximate the two-photon ePSF by simpler three-dimensional peak functions such as the two-dimensional Gauss-Lorentz distribution or the asymmetrical three-dimensional Gauss distribution (16). Indeed, the experimental ePSFs measured with our setup could be fitted by asymmetrical three-dimensional Gauss functions. The ePSFs were measured by collecting the local three-dimensional fluorescence signal of small labeled polystyrene beads whose diameter (100 nm) was below the resolution limit of our setup.

To characterize the resolution of the single-beam PMT compared to the multibeam CCD setup, we performed ePSF measurements with both methods in thick agarose gels. This was done at different excitation wavelengths in the range of 720–920 nm, with two different types of labeled beads (fluorescence maximum at 440 and 515 nm), at different penetration depths, and with two different lenses, i.e., a 20× high-working-distance water-immersion objective (NA = 0.95) and a 100× low-working-distance oil-immersion objective (NA = 1.4). The lateral and axial dimensions of the ePSFs were determined from one-dimensional Gaussian fits of the respective x, y, and z profiles. Thereby, we considered the maximum extension of the ePSF in each direction for evaluation.

In conformity with the diffraction theory (16), both the lateral and the axial resolution decreased with increasing excitation wavelength, whereas neither the emission wavelength nor the penetration depth had a measurable effect on the spatial resolution (Supplementary Table 1).

The dimensions of the theoretical PSF, calculated using paraxial approximation, corresponded very well to the spatial resolution measured in agarose. At an excitation wavelength of 800 nm, the calculated axial resolution was 347 nm, and the lateral resolution 1.47 μm, whereas the measured values were (lateral) 344 ± 14 nm and (axial) 1.41 ± 0.09 μm, respectively (Fig. 1, *A* and *B*).

The maximum penetration depth in agarose measured using the 20× objective was larger than 900 μm, i.e., the thickness of the sample, for both setups. The spatial resolution in this depth measured using green fluorescent beads (fluorescence maximum at 515 nm) excited at 780 nm amounted to 364 ± 12 nm (lateral) and 1.42 ± 0.02 μm (axial) for the multibeam CCD setup and to 363 ± 16 nm (lateral) and 1.44 ± 0.07 μm (axial) for the single-beam PMT setup. Thus, in agarose the loss of resolution caused by imaging depth was less than 2.5%.

The spatial resolution measured with a high-NA objective in agarose at 780-nm excitation wavelength (fluorescence maximum 515 nm) was 207 ± 7 nm (lateral) and 814 ± 31 nm (axial) for the multibeam CCD setup and 209 ± 10 nm (lateral) and 817 ± 16 nm (axial) for the single-beam PMT setup. These values correspond to already published results using the same or similar lenses (20,21). The maximum penetration depth was limited to 100 μm by the working distance of the objective.

Despite its very high spatial resolution, the 100× objective is inadequate for imaging biological samples because of its short working distance and the need for oil immersion. Thus, all further experiments were performed with the more appropriate 20× water-immersion objective.

For directly comparing the spatial resolution of the single- and multibeam excitation mode, we used the CCD camera as detector for both modes to rule out differences introduced by the detection method. We performed ePSF measurements in agarose using 3-mW laser power in the focus of each beam and 12-μs pixel time. Independent of the number of laser beams (1, 2, ... 64) used, all experiments yielded the same axial and lateral resolution. By using the 20× objective combined with a twofold magnification of the fluorescence image, a pixel resolution of 161 nm on the CCD chip and of 141 nm on the reconstructed PMT image was obtained. For the 100× objective, the pixel resolution was 65 nm on the CCD chip and 56 nm on the PMT image. The steps between two consecutive optical slices were adjusted to 300 nm in all ePSF measurements.

Spatial resolution decreases with imaging depth and sample complexity

Transparent media such as agarose are advantageous for characterization of the maximum optical performance of imaging devices. However, there are large differences between this ideal model and genuine probes. To test the influence of optical density and refraction-index variation, we performed ePSF experiments on two tissue types of particular interest, i.e., OHBS and lymph nodes. Fig. 1, *C* and *D*, depicts representative results for depth-dependent ePSFs in OHBS, whereas *E* and *F* show typical values in the lymph node. The xy region considered for evaluation was relatively small (15 × 15 μm^2) because the heterogeneous surface (nonplanar in the range of several micrometers), which is typical for brain slices and lymph nodes, affects penetration depth and resolution. Only when one is measuring small xy regions is the imaging depth nearly uniform over the whole image.

The spatial resolution in biological samples was strongly influenced not only by the penetration depth but also by the

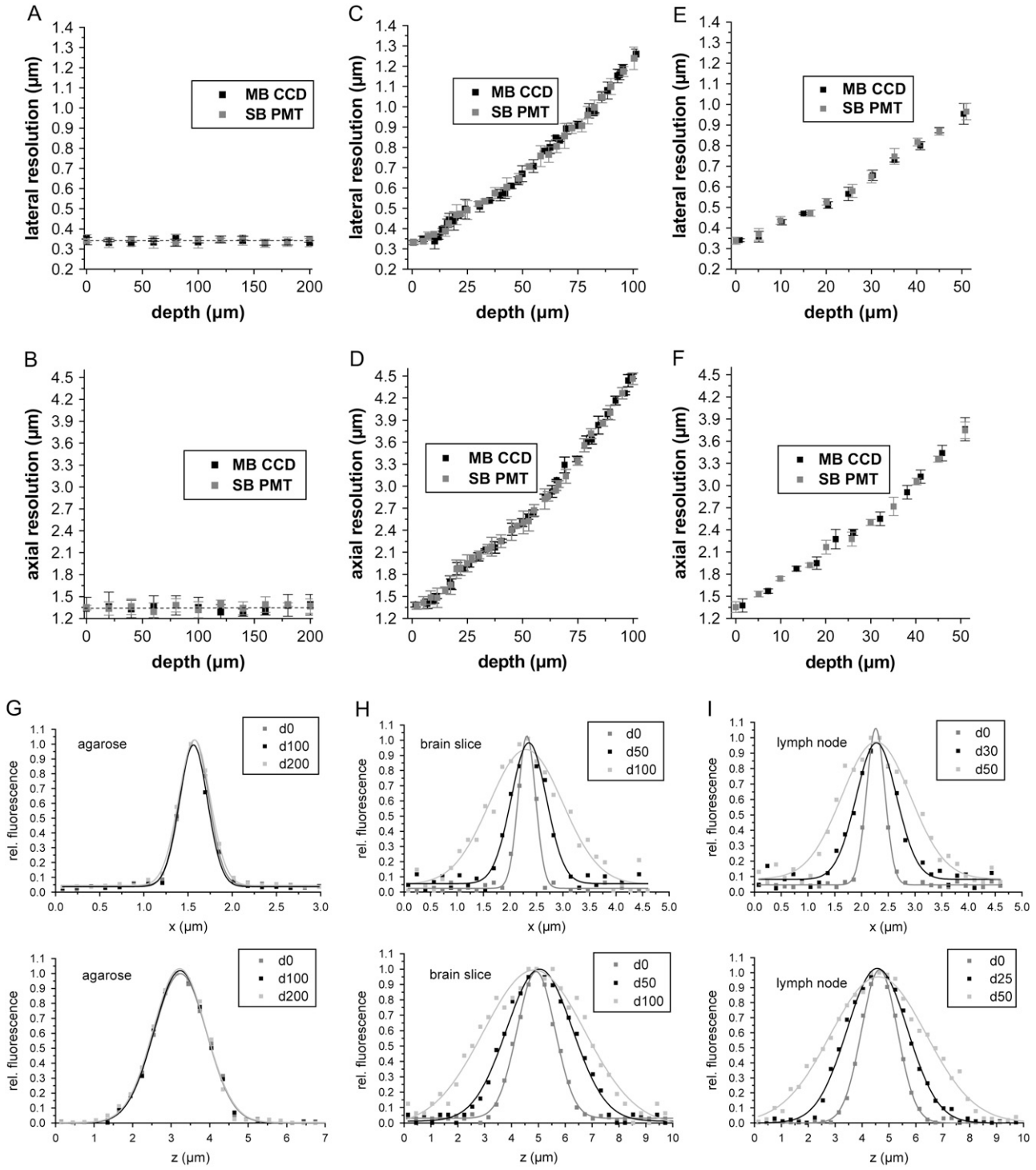

FIGURE 1 Dependence of the spatial (lateral and axial) resolution on the penetration depth measured in (*A* and *B*) agarose, (*C* and *D*) brain tissue, and (*E* and *F*) lymph nodes with both the single-beam PMT and the multibeam CCD setup. Typical lateral and axial profiles of experimental ePSF are shown in three different depths for (*G*) agarose, (*H*) brain tissue, and (*I*) lymph node. The ePSF were measured using green fluorescent beads (emission maximum 515 nm) excited at 800 nm. Each value of the spatial resolution was calculated as the average over 6–15 data points.

tissue constitution, which varied strongly even within the same sample (Figs. 1 and 2). To quantify this effect, we comparatively measured the dependence of the spatial resolution on the penetration depth in lymph nodes and OHBS in regions containing either mainly axons or somata. Representative results are depicted in Fig. 2. Importantly, the decrease in resolution was independent of the detection device. Laser powers of 3 mW/beam were used in all ePSF experiments within biological

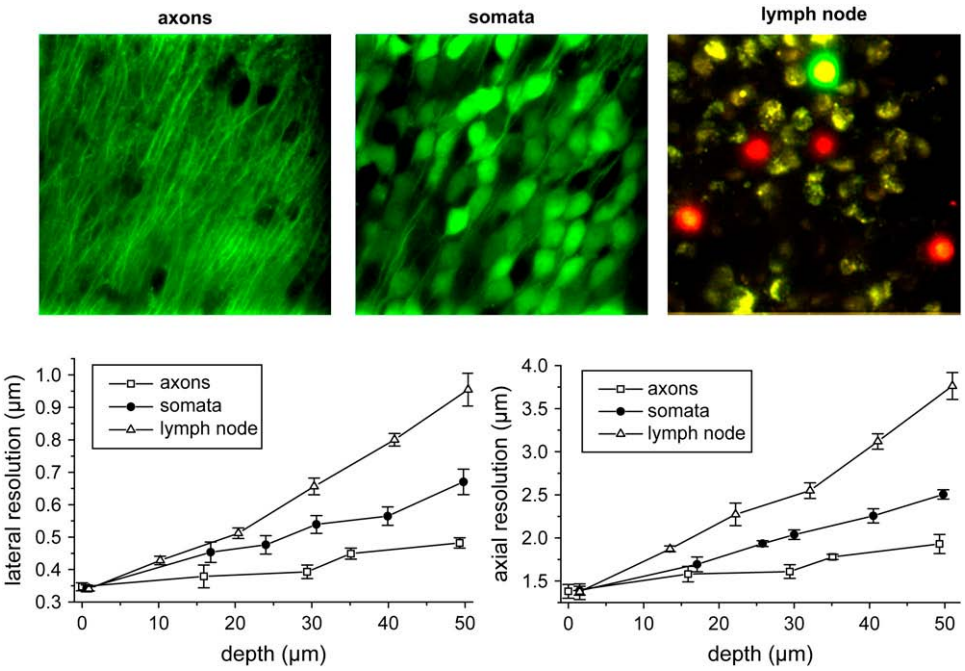

FIGURE 2 Dependence of the spatial resolution on the penetration depth in lymph nodes and in brain slice regions containing axons and somata, respectively. The ePSF experiments were performed with green fluorescent beads (emission maximum 515 nm) using the multibeam CCD setup at 800 nm excitation wavelength. Images show representative pictures of brain slices from Thy-1-EYFP transgenic animals or lymph nodes from wt animals where red and green leukocytes had been adoptively transferred before imaging. Please note the abundance of cell bodies in lymph nodes (either from transferred red or green cells or from endogenous autofluorescent cells) and brain regions with somata, whereas axon-rich brain areas display a relatively low number of (*black*, i.e., EYFP-negative) cell bodies.

samples, no matter which detection method was used. The pixel time for CCD-based measurements ranged between 12 and 21 μs, whereas that for PMT measurements was between 70 and 160 μs/pixel. Thus, the PMT images were acquired by scanning significantly more slowly to collect enough signal per pixel.

Deconvolution with depth-dependent ePSF

Mathematical postprocessing of fluorescence images leads to a considerable gain of information and optical quality. One of the most efficient techniques is the three-dimensional deconvolution of raw data, i.e., *z*-stacks of fluorescence images, with corresponding PSFs (22). Currently, three-dimensional deconvolution is performed using a constant PSF either calculated from the technical data of the microscope or evaluated from the fluorescence three-dimensional signal of a punctiform object, usually measured in an ideal sample such as agarose. However, we observed that the PSF was not a constant parameter but rather was strongly influenced by the constitution of the sample and by the penetration depth (Fig. 2). This insight gave rise to the question of whether a three-dimensional deconvolution performed with a depth-dependent PSF typical for the imaged sample would lead to an improvement of the postprocessed data as compared to the currently used three-dimensional deconvolution techniques.

Thus, we imaged a region of a 78-μm-thick OHBS that was fixed between two coverslips, from both sides. In this way, we collected two mirrored three-dimensional stacks of the same region, so that the first image (Fig. 3 *F*) at the surface of one stack corresponded to the last image (Fig. 3 *C*), i.e., deepest layer, of the other. This allowed imaging the same region within a biological tissue either through 75 μm of overlying tissue (the usual approach in deep tissue in vivo imaging) or directly from the other side. Thus, we could also produce the same picture without any tissue layer disturbing the image, giving the optimal result obtainable within this sample. Moreover, we measured the depth-dependent ePSF in both three-dimensional stacks, so that for each fluorescence image the corresponding ePSF was known (Fig. 3, *A–C, F*). The ePSF used for deconvolution was averaged within each *xy* plane but was specifically taken in each *z*-position.

As expected, increasing penetration depth degraded both the resolution and the optical quality of the fluorescence images (Fig. 3, *A–C*). Even if images *C* and *F* in Fig. 3 show the same OHBS area, because of scattering, the quality of image *C* collected through 75 μm of tissue is considerably lower than that of image *F*, which was collected through only 3 μm of tissue from the opposite side of the sample.

By three-dimensional deconvolution based on the ePSF measured in agarose, which corresponded to the calculated PSF, the amount of detail was not evidently larger than that in the original image (Fig. 3, *C* and *D*), although the noise increased dramatically (Fig. 3, *D* and *G*). Three-dimensional deconvolution based on the penetration depth-dependent ePSF of brain tissue delivered an even higher optical quality than the direct image of the same area, which was collected through only 3 μm of tissue (Fig. 3, *E* and *F*). Thus, postprocessing using the depth-corrected PSF can generate images from planes deep inside tissue with a resolution comparable to that obtained by imaging near the surface.

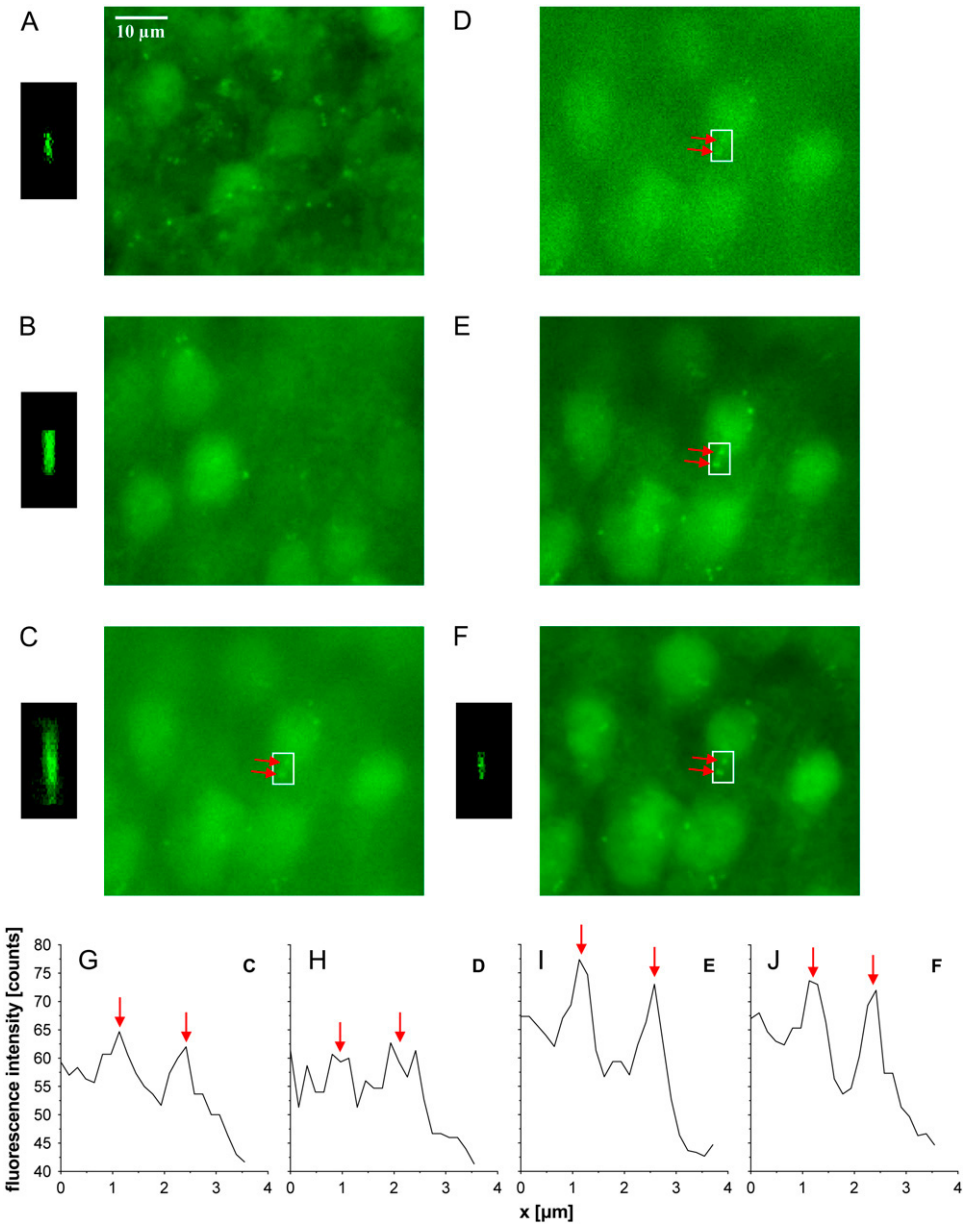

FIGURE 3 Deconvolution with depth-dependent ePSF allows restoration of images from deep tissue layers to the quality level of surface data. Fluorescence images of a 78-μm-thick brain slice and corresponding *xz* cross sections of the in situ measured ePSF: (*A*) at the surface, (*B*) in 37 μm depth, and (*C*) in 75 μm depth. (*D*) Three-dimensional deconvolved image of *C* using the ePSF measured at the surface (identical to the ePSF measured in agarose). (*E*) Three-dimensional deconvolution of *C* using the ePSF measured in 75-μm depth. (*F*) The same layer as *C* but imaged from the other side of the brain slice, i.e., through a brain tissue layer of only 3 μm thickness. The diagrams *G, H, I*, and *J* represent intensity profiles along a line through the two bright spots indicated by red arrows in the images *C–F*. For optimal deconvolution, the heights of maxima as well as height of the minimum have to be as close as possible to the ''perfect'' image in *F*. The experiments were performed using the multibeam CCD setup at an excitation wavelength of 800 nm. The *z*-step between two consecutive optical slices was 500 nm.

Maximum penetration depth and SNR

Many relevant biological phenomena happen at a considerable depth within highly scattering biological tissues. Thus, the maximum penetration depth at which useful dynamic, high-resolution images can still be generated is a central feature of tissue imaging devices.

Thus, we measured the maximum penetration depth in OHBS, both with the multibeam CCD and with the single-beam PMT setup. The maximum penetration depth reached ~500 μm for the single-beam PMT setup and ~300 μm for the multibeam CCD setup. Consequently, the fluorescence signal strongly decreased with increasing penetration depth independent of the detection device. However, this decrease was more rapid for the multibeam CCD than for the single-beam PMT system (Fig. 4 *A*).

It is evident that the maximum penetration depth is reached when the fluorescence signal decreases to the level of the background noise and, thus, cannot be distinguished from it any more. The parameter that defines the relation between the fluorescence signal and the background noise is the SNR, which in maximum penetration depth reaches the value 1 (SNR = 1) by definition.

With the multibeam CCD setup, the SNR value of 1 was reached at 310 μm depth, whereas with the single-beam PMT setup this happened at 510 μm depth (Fig. 4 *B*). It is noteworthy that down to a penetration depth of ~150 μm the SNR values were similar for both setups, and the reduction of the SNR was moderate; i.e., the SNR decreased 45% in both systems within the first 150 μm of penetration into the sample. Loss of SNR was accelerated at higher depths. In the

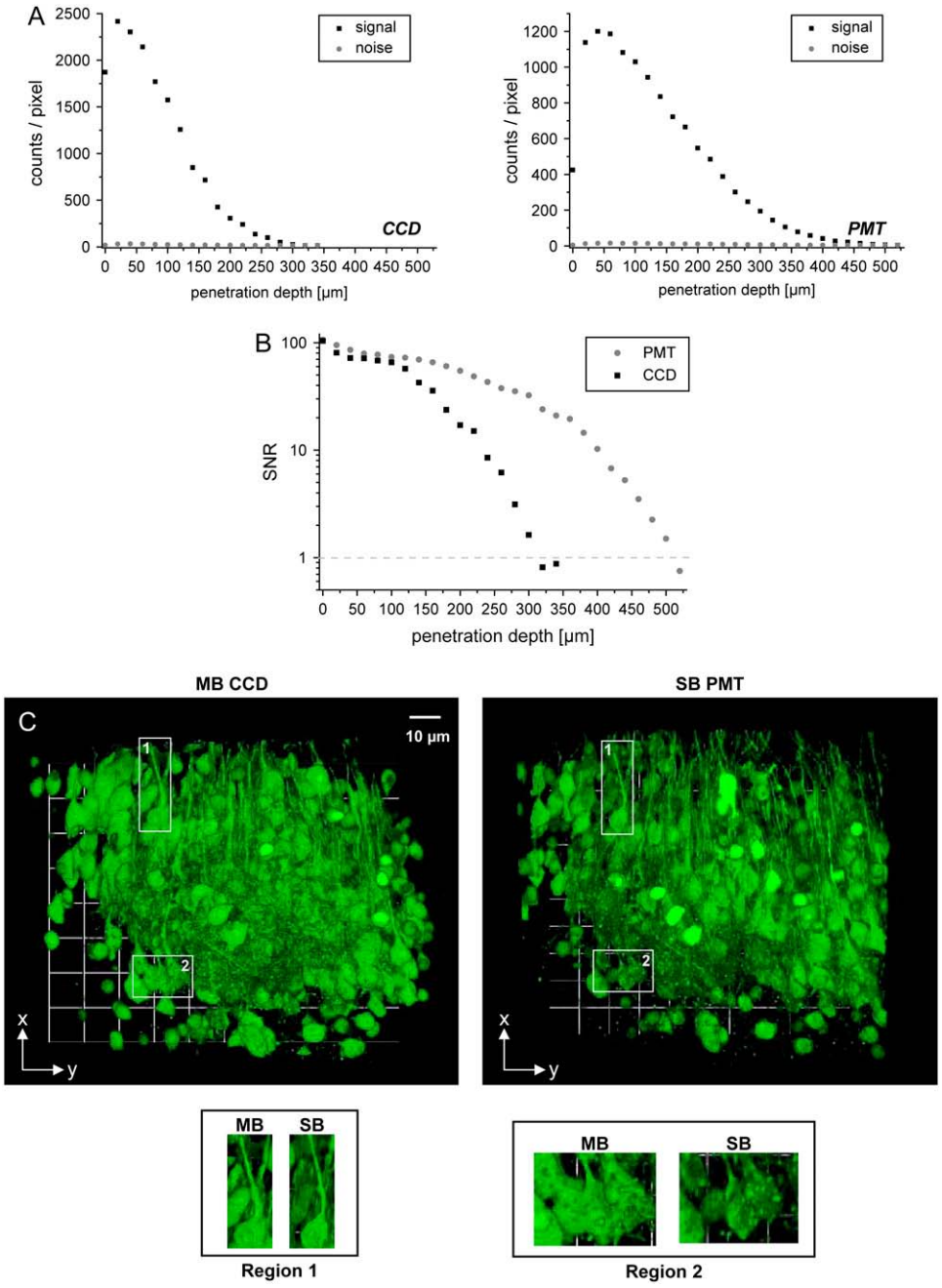

FIGURE 4 (*A*) Dependence of the fluorescence signal and of the background noise on the penetration depth measured with the multibeam CCD or single-beam PMT setup. Because of the truncation of the PSF at the sample surface, the fluorescence signal in this depth is lower than that at 20 μm depth. (*B*) Dependence of the SNR on the penetration depth. The *z*-step between two consecutive optical slices was 2 μm (imaged region 300 $\times$ 300 μm^2). (*C*) Comparison between the multibeam CCD and the single-beam PMT setup on the example of a three-dimensional reconstruction of an EYFP brain slice region. A Thy-1-EYFP brain slice of 166 μm thickness was imaged either with the multifocal CCD or the single-beam PMT setup and subsequently voxel-rendered with a 1-μm *z*-spacing. The small images show zoomed views of two identical regions in both stacks, revealing almost identical optical performance and content. The excitation wavelength was 920 nm in all experiments.

range 150–300 μm depth, 96% of the SNR was lost with CCD and only 71% with PMT detection (Fig. 4 *B*). This was the main reason for the higher penetration depth of the PMT detection method. Consequently, within depths of 150–200 μm, CCD and PMT performed equally well. As a result, images obtained from both devices in this region show a comparable degree of optical content and resolution (Fig. 4 *C*). Fluorescence images of a 166-μm-thick sample of a brain slice obtained with the single-beam PMT setup appeared only slightly crisper (Fig. 4 *C*).

A laser power of 2 mW/beam was chosen for all SNR experiments. The pixel time used for CCD-based imaging was 6 μs/pixel (pixel size 322.5 $\times$ 322.5 nm^2), and that for single-beam excitation with a PMT as detector amounted to 5 μs/pixel (pixel size 293 $\times$ 293 nm^2). The scanned sample region was 300 $\times$ 300 μm^2 in both cases.

Imaging speed

Thus, the main advantage of the single-beam PMT setup over the multibeam CCD device is the larger penetration depth in strongly scattering samples because of a better SNR gradient (Fig. 4). However, besides imaging in deep tissue, visualizing the dynamics of biological phenomena represents

an equally important challenge for bioimaging (11,23). In terms of imaging speed, the multibeam CCD technique is evidently superior to the state-of-the-art PMT method. To obtain images of equal quality and dynamic range, a 150 × 150 μm^2 area was imaged within 5000 ms with the single-beam PMT setup and within only 83 ms with the multibeam CCD setup. Thus, CCD detection has a clear advantage over the single-beam PMT when high imaging speed is relevant. A laser power of 2 mW/beam and pixel times of 0.4 μs (pixel size 322.5 × 322.5 nm^2) for the CCD and 27 μs (pixel size 293 × 293 nm^2) for the PMT were used, similar to the SNR experiments. Imaging depths between 0 and 50 μm were taken into account.

To quantify the speed of the multibeam CCD system at the outermost limit, we imaged the fluorescence of blood flow in vessels of living mice two- and three-dimensionally, in one color and in two different spectral channels, simultaneously (Fig. 5). Although for the single-color experiments only one CCD camera was necessary, for the dual-color experiments fluorescence was imaged onto two synchronized CCD cameras after being spectrally separated by a dichroic mirror.

By this approach, individual cellular and subcellular fragments of blood (erythrocytes, white cells, and platelets) could be visualized in almost natural (i.e., round) shape, and many individual steps of white cells rolling on the surface of vessels were captured (Fig. 5 *A, movies 1* and *2*). In rolling cells, subcellular structures could sometimes be resolved, making it possible to observe barrel rolling of the cell body over the vessel surface (Fig. 5 *C, movie 5*).

Because the applied intravital dye Rhodamine-6G slowly diffused out of the blood vessels, it also stained cells in the surrounding connective tissue. Thus, this approach allowed simultaneous visualization of the ~100× slower autonomous three-dimensional movement of cells in tissue, next to the fast transport of cells in blood vessels (Fig. 5 *B, movie 3*). The two-color image sequence shows individual rolling steps of cells in different colors separated from other cellular blood components that were still well resolved and appeared in yellow (Fig. 5 *C, movies 5* and *6*). Three-dimensional rendering allowed reconstruction of whole cell bodies in the free bloodstream. However, because of the fast transport, these cells appeared distorted (Fig. 5 *D, movies 3, 4*, and *7*). In addition, in two-color three-dimensional experiments, we reached the border of technical feasibility with this setup because after spectral separation the SNR in both channels was close to the value of 1, making it difficult to separate the signal from background noise.

DISCUSSION

MPM of live cells in explanted tissues or living animals today is a rapidly developing field (6). Consequently, imaging hardware is also developing apace. In particular, tunable Ti:Sa lasers as light source have seen an enormous improvement from early machines, which covered a complete laboratory desk and required an expert to change the wavelength, to contemporary travel-bag-sized turn-key systems that provide a wide tuning range and easy-to-use computer interfaces for control. Also, the output power of these lasers has increased dramatically. Current models provide >2 W average power at 800 nm emission, and the most recent developments will provide as much as 2.5–3 W including >1 W at wavelengths of >900 nm.

As a result, conventional single-beam scanheads have built-in attenuators that decrease the laser power reaching the sample, typically by 99%, to avoid bleaching and thermal sample destruction. The multibeam scanhead used in this study distributes the available laser power onto up to 64 beams, which is only 1.7% per beam. This is still enough for efficient two-photon excitation but below the destructive level for most applications. Consequently, the laser generally runs at full power, and thus, much more fluorescence light per time is generated

However, multifocal illumination requires whole-field detection of the fluorescence with a CCD camera. Thus, it was necessary to compare the optical performance of this method with the usually applied PMT detection of single-beam scanning setups. It was generally assumed that detection with a CCD would be inferior to PMT detection because there is no method to suppress scattered photons (11). We were, therefore, surprised to find that neither the ePSF nor the loss of resolution with imaging depth showed differences for both detection devices down to imaging depths of 200 μm in optically dense tissue. Our experiments show that the development of the SNR is responsible for the differences in maximum penetration depth. Although the SNR value for the CCD decayed more rapidly than that of the PMT, it was still well above 1 at 200 μm, where signals are lost in the background noise. Only in very deep regions (>310 μm) was the CCD no longer able to differentiate signals, a point that was not reached for the PMT until 500 μm imaging depth. Because the majority of imaging studies record cellular movements at 100–200 μm below the surface, e.g., of lymph nodes (24–26) or the brain (27,28), our work shows that in this area CCD detection is equivalent to PMT detection. Additionally, CCD detection will benefit from more powerful lasers, which will enhance the SNR and thus make it possible to reach deeper regions, although this can not be expected for PMT because of phototoxicity issues. Because the scanhead used here can run PMT or CCD detection, it is not necessary to choose one system. Instead, the optimal detection device can be used for each problem under investigation.

Our study also demonstrates that the resolution of two-photon imaging in biological tissues is a function not only of imaging depth but also of the environment where imaging is performed. In brain areas where axons are predominant, loss of resolution was much less pronounced than in areas with high numbers of somata. The most difficult tissues studied here were lymph nodes, which destroyed the depth-dependent two-photon ePSF very rapidly. This argues for the concept

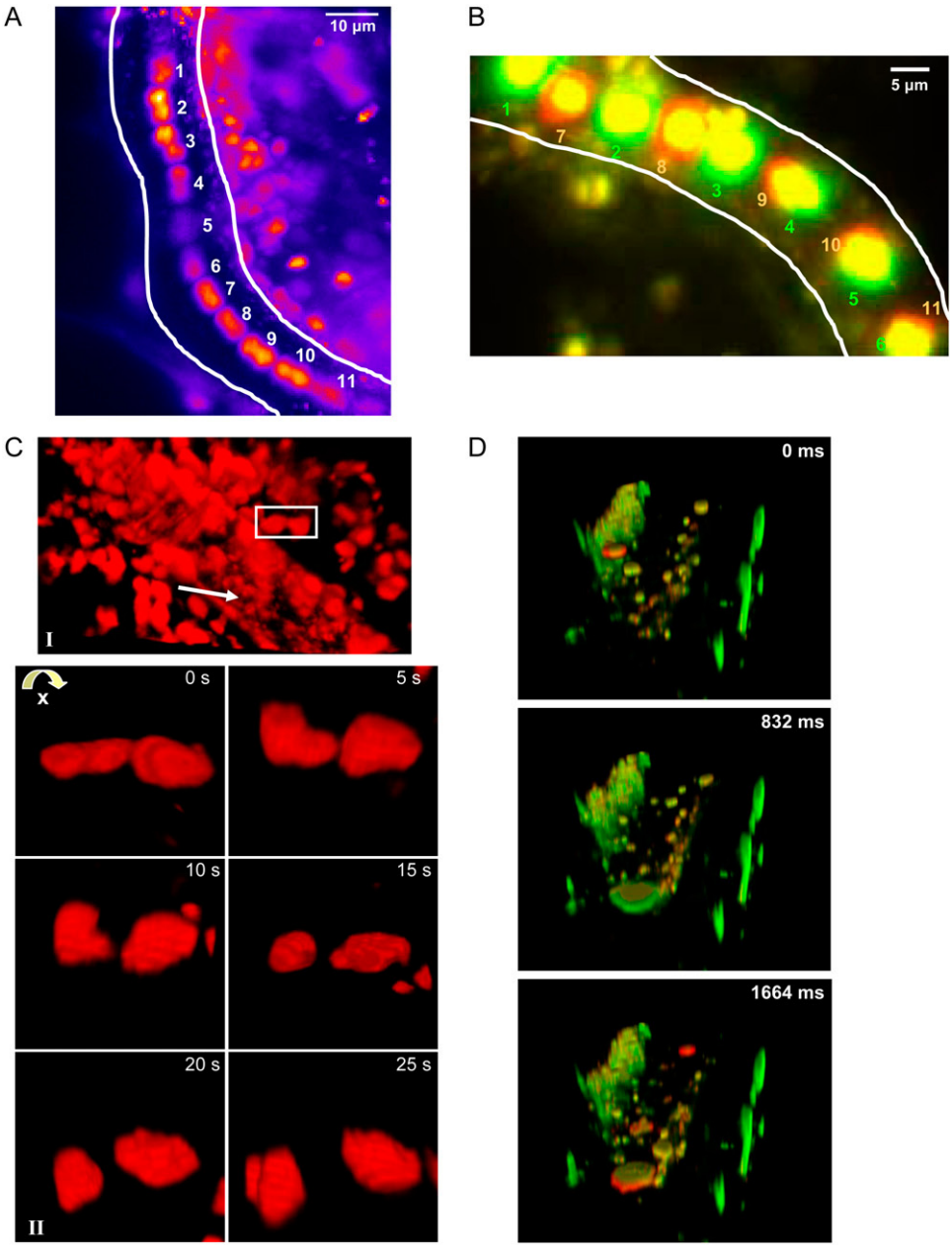

FIGURE 5 Imaging blood flow in mice in real time with a multibeam CCD setup. Dual-color images were detected simultaneously with two independent CCD cameras based on color splitting by a 570-nm-cutoff dichroic mirror. (*A*) Time projection over 11 single-color two-dimensional fluorescence images of a blood vessel and surrounding tissue stained by i.v. injection of Rhodamine-6G. The time delay between two consecutive numbers was 50 ms. Shown is a cell doublet rolling on the surface of the vessel (*white outlines*). Images were taken from movies 1 and 2. (*B*) Time projection of 11 dual-color two-dimensional fluorescence images of a blood vessel (*white outlines*) stained with Rhodamine 6G (*yellow*). Spleen cells previously stained either with CFSE (*green*) or CTO (*red*) and additionally injected into the mouse are represented green and red, respectively, because they were detected by only one of the two CCD cameras. The fact that blood cells stained with Rhodamine-6G only appear yellow indicates their simultaneous detection in both cameras and thus proves the synchronicity of the system. The green numbers indicate the position of a CFSE-stained cell at six different time points, whereas the red numbers indicate the position of a CTO-stained cell at five subsequent time points. The time delay between two consecutive numbers is 50 ms. Images were taken from movies 5 and 6. (*C I*) Three-dimensional visualization of the fluorescence of a blood vessel and surrounding tissue-resident cells, which were stained with Rhodamine 6G as described above. (*C II*) Image series representing the two cells framed in *C I* at six different time points during a 180° rotation around the *x* axis. The *z*-stacks used for the three-dimensional representation contained 21 frames each, separated by 1 μm. Time delay between two consecutive *z*-stacks was 5 s. Images were taken from movies 3 and 4. (*D*) Three-dimensional representations of the dual-color fluorescence of a blood vessel in a mouse prepared as described above at three different time points. The time delay between two consecutive *z*-stacks was 800 ms. The *z*-stacks used for the three-dimensional representations contained 16 frames each, separated by 2 μm. Images were taken from movie 7. In all experiments: minimum exposure time = 28 ms, excitation wavelength = 800 nm. The minimum delay between two consecutive images was limited by the readout time of the CCD chip.

that tissues with a predominance of cell nuclei, such as brain in regions with somata but especially lymph nodes, where $>1{\cdot}10^6$ nuclei are located within $\sim$1 μl volume, are particularly difficult for deep-tissue imaging. Thus, it was very encouraging to find that poor-quality images from deep regions could be deconvolved efficiently to an image quality that can usually be obtained only directly below the surface of tissues.

We demonstrate here that this deconvolution is possible only if an ePSF that corresponds to the imaged tissue and, especially, the imaged depth is used for image restoration. Deconvolution based on a general ePSF calculated for the optical setup produced unusable results, as already attempted elsewhere (29). Unfortunately, currently available deconvolution software does not account for depth-dependent PSF. In addition, mathematical deconvolution is still very time

consuming, making it difficult to reconstruct multichannel, multistack time series. Software development to overcome these barriers would thus be desirable. Future work needs to show whether typical tissue-type- and depth-related ePSFs can be obtained and used for deconvolution or whether ePSFs must always be specifically determined for the investigated sample. Even if this turns out to be necessary for optimal image quality, it is not required to provide artificial sub-resolution particles within the sample. Instead, our experience shows that the use of small endogenous structures as a reference is possible.

Finally, we could demonstrate the potential of fast two-photon imaging. This allowed us to visualize autonomous movements of perivascular cells in time and space. The identity of these cells is currently unclear. Based on their shape and size, macrophages or lymphocytes appear likely. It will be very interesting to see the change in migratory behavior of these cells when a local trigger, e.g., injury or infection, occurs.

However, even this setup was not able to reconstruct the three-dimensional shape of freely flowing blood cells satisfyingly. This was based on reaching the technical limits. At the given staining protocol and illumination regime, single erythrocytes or leukocytes did simply not produce enough fluorescence photons to allow for even shorter illumination time, which would be the basis for more rapid *z*-stacks. Thus, future developments should improve the brightness of labels. Also higher laser power or the use of even more beams in parallel will enable faster image acquisition times. Finally a rapid and reliable *z*-stepper could be obtained by fixing the distance between object and lens and shift the focal plane by moving the tube lens rather than the objective. This would avoid motion and compression artifacts and allow for rapid *z*-scanning.

In summary, we have shown here that multifocal illumination opens the way to fast, yet highly accurate, two-photon microscopy. Future developments will prove the power of this approach for biomedical research.

SUPPLEMENTARY MATERIAL

To view all of the supplemental files associated with this article, visit www.biophysj.org.

This study was supported by the Deutsche Forschungsgemeinschaft (SPP 1160 (GU 769/1-1 and GU 769/1-2) to M.G.) and by the German Ministry for Education and Research (BMBF, Bioprofile) to M.G., H.S., and V.A. We thank Christof Maul for critical reading of the manuscript.

V.A. and H.S. work for LaVision Biotec GmbH, Bielefeld, Germany, which produces the multiplexing scan-head TriMScope used in the experiments presented in this work.

REFERENCES

1. Lichtman, J. W., and J. A. Conchello. 2005. Fluorescence microscopy. *Nat. Methods.* 2:910–919.
2. Sumen, C., T. R. Mempel, I. B. Mazo, and U. H. von Andrian. 2004. Intravital microscopy; visualizing immunity in context. *Immunity.* 21: 315–329.
3. von Andrian, U. H., and C. M'Rini. 1998. In situ analysis of lymphocyte migration to lymph nodes. *Cell Adhes. Commun.* 6: 85–96.
4. Halin, C., M. J. Rodrigo, C. Sumen, and U. H. von Andrian. 2005. In vivo imaging of lymphocyte trafficking. *Annu. Rev. Cell Dev. Biol.* 21:581–603.
5. Gunzer, M., C. Weishaupt, A. Hillmer, Y. Basoglu, P. Friedl, K. E. Dittmar, W. Kolanus, G. Varga, and S. Grabbe. 2004. A spectrum of biophysical interaction modes between T cells and different antigen presenting cells during priming in 3-D collagen and in vivo. *Blood.* 104:2801–2809.
6. Cahalan, M. D., I. Parker, S. H. Wei, and M. J. Miller. 2002. Two-photon tissue imaging: seeing the immune system in a fresh light. *Nature Rev. Immunol.* 2:872–880.
7. Konig, K. 2000. Multiphoton microscopy in life sciences. *J. Microsc.* 200:83–104.
8. Denk, W., J. H. Strickler, and W. W. Webb. 1990. Two-photon laser scanning fluorescence microscopy. *Science.* 248:73–76.
9. Helmchen, F., and W. Denk. 2005. Deep tissue two-photon microscopy. *Nat. Methods.* 2:932–940.
10. Hasan, M. T., R. W. Friedrich, T. Euler, M. E. Larkum, G. G. Giese, M. Both, J. Duebel, J. Waters, H. Bujard, O. Griesbeck, R. Y. Tsien, T. Nagai, A. Miyawaki, and W. Denk. 2004. Functional fluorescent $Ca2^{+}$ indicator proteins in transgenic mice under TET control. *PLoS Biol.* 2:E163.
11. Germain, R. N., M. J. Miller, M. L. Dustin, and M. C. Nussenzweig. 2006. Dynamic imaging of the immune system: progress, pitfalls and promise. *Nature Rev. Immunol.* 6:497–507.
12. Reichardt, P., and M. Gunzer. 2006. The biophysics of T lymphocyte activation in vitro and in vivo. *In* Cell Cell Communication in the Nervous and Immune System. B.Schraven, E.Gundelfinger, and C.Seidenbecher, editors. Springer-Verlag, Berlin. 199–218.
13. Larson, D. R., W. R. Zipfel, R. M. Williams, S. W. Clark, M. P. Bruchez, F. W. Wise, and W. W. Webb. 2003. Water-soluble quantum dots for multiphoton fluorescence imaging in vivo. *Science.* 300:1434–1436.
14. Nielsen, T., M. Fricke, D. Hellweg, and P. Andresen. 2001. High efficiency beam splitter for multifocal multiphoton microscopy. *J. Microsc.* 201:368–376.
15. Rueckel, M., J. A. Mack-Bucher, and W. Denk. 2006. Adaptive wavefront correction in two-photon microscopy using coherence-gated wavefront sensing. *Proc. Natl. Acad. Sci. USA.* 103:17137–17142.
16. Gu, M. 2000. Advanced Optical Imaging Theory. Springer, Berlin.
17. Hell, S. W., G. Reiner, C. Cremer, and E. H. K. Stelzer. 1993. Aberrations in confocal fluorescence microscopy induced by mismatches in refractive index. *J. Microsc.* 196:391–405.
18. Török, P., and F.-J. Kao. 2002. Point-spread function reconstruction in high-aperture lenses focusing ultra-short laser pulses. *Optics Comm.* 213:97–103.
19. Squire, J., and M. Müller. 2001. High resolution nonlinear microscopy: A review of sources and methods for achieving optimal imaging. *Rev. Sci. Instrum.* 72:2855–2867.
20. Kano, H., H. van du Voort, M. Schrader, G. van Kempen, and S. W. Hell. 1996. Avalanche photodiode detection with object scanning and image restoration provides 2–4 fold resolution increase in two-photon fluorescence microscope. *Bioimaging.* 4:187–197.
21. Diaspro, A., G. Chirico, F. Federici, F. Cannone, S. Beretta, and M. Robello. 2001. Two-photon microscopy and spectroscopy based on a compact confocal scanning head. *J. Biomed. Opt.* 6:300–310.
22. Conchello, J. A., and J. W. Lichtman. 2005. Optical sectioning microscopy. *Nat. Methods.* 2:920–931.
23. Kurtz, R., M. Fricke, J. Kalb, P. Tinnefeld, and M. Sauer. 2006. Application of multiline two-photon microscopy to functional in vivo imaging. *J. Neurosci. Methods.* 151:276–286.

24. Bajenoff, M., B. Breart, A. Y. Huang, H. Qi, J. Cazareth, V. M. Braud, R. N. Germain, and N. Glaichenhaus. 2006. Natural killer cell behavior in lymph nodes revealed by static and real-time imaging. *J. Exp. Med.* 203:619–631.

25. Castellino, F., A. Y. Huang, G. tan-Bonnet, S. Stoll, C. Scheinecker, and R. N. Germain. 2006. Chemokines enhance immunity by guiding naive CD8+ T cells to sites of CD4+ T cell-dendritic cell interaction. *Nature*. 440:890–895.

26. Qi, H., J. G. Egen, A. Y. Huang, and R. N. Germain. 2006. Extrafollicular activation of lymph node B cells by antigen-bearing dendritic cells. *Science*. 312:1672–1676.

27. Nimmerjahn, A., F. Kirchhoff, and F. Helmchen. 2005. Resting microglial cells are highly dynamic surveillants of brain parenchyma in vivo. *Science*. 308:1314–1318.

28. Davalos, D., J. Grutzendler, G. Yang, J. V. Kim, Y. Zuo, S. Jung, D. R. Littman, M. L. Dustin, and W. B. Gan. 2005. ATP mediates rapid microglial response to local brain injury in vivo. *Nat. Neurosci*. 8:752–758.

29. Shimizu, K., K. Tochio, and Y. Kato. 2005. Improvement of transcutaneous fluorescent images with a depth-dependent point-spread function. *Appl. Opt.* 44:2154–2161.

30. Neumann, J., M. Gunzer, H. O. Gutzeit, O. Ullrich, K. G. Reymann, and K. Dinkel. 2006. Microglia provide neuroprotection after Ischemia. *FASEB J*. 20:714–716.

31. Feng, G., R. H. Mellor, M. Bernstein, C. Keller-Peck, Q. T. Nguyen, M. Wallace, J. M. Nerbonne, J. W. Lichtman, and J. R. Sanes. 2000. Imaging neuronal subsets in transgenic mice expressing multiple spectral variants of GFP. *Neuron*. 28:41–51.